Low Temperature Plasma
Technology Laboratory

Collisional, magnetic, and nonlinear skin effect in RF plasmas

Francis F. Chen

Electrical Engineering Department, University of California, Los Angeles, California 90095-1594

LTP-011 November, 2000

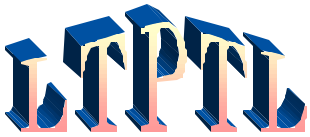

Electrical Engineering Department
Los Angeles, California 90095-1594

Collisional, magnetic, and nonlinear skin effect in RF plasmas

Francis F. Chen

Electrical Engineering Department, University of California, Los Angeles, California 90095-1594

ABSTRACT

The penetration of RF energy into cylindrical devices is relevant to the production of uniform plasmas for etching and deposition processes in the production of semiconductor circuits. The so-called "anomalous skin effect" has been invoked to explain irregularities not predicted by classical electromagnetic theory. These expectations are summarized for the collisionality regimes of interest, and new results are given for non-kinetic effects caused by small DC magnetic fields and the ponderomotive force.

I. CLASSICAL vs. ANOMALOUS SKIN EFFECT

Inductively coupled plasmas (ICPs) are commonly used in plasma processing of semiconductor microchips, but the mechanism by which the applied radiofrequency (RF) energy is distributed to produce a uniform density is not well understood. In simplest terms, the propagation of electromagnetic waves into a plasma follows the dispersion relation

$$c^2k^2 = w^2 - w_p^2, \tag{1}$$

where ω_p is the plasma frequency $(ne^2/e_0m)^{1/2}$. Since $\omega << \omega_p$ is well satisfied in ICPs, the propagation constant k is imaginary, with the magnitude

$$k_s \equiv w_p/c, \tag{2}$$

leading to the classical skin depth

$$d_c = c/w_p. \tag{3}$$

However, this e-folding distance is usually so small that ionization should be concentrated near the antenna, creating a much more nonuniform plasma density n than is observed. Furthermore, the RF field has been seen to decay non-monotonically away from the antenna, first by Demirkhanov et al.[1] and Joye and Schneider[2], and more recently by Godyak and coworkers[3-6]. These observations spawned a theory of "anomalous skin effect" by Weibel[7] and Sayasov[8] based on the following kinetic effect. When the collisionality is sufficiently low, electrons impinging on the wall sheath at a glancing angle can stay within the skin depth to be accelerated to hyperthermal energies by the RF electric field of the antenna. These fast electrons can then scatter out of the skin region and transport an ionizing current to regions far from the wall, causing non-local power deposition[3,9]. Theory and experiment on the "anomalous" skin effect, which refers only to anomalies related to kinetic effects, have been extensively reviewed by Kolobov and Economou[10] and by Lieberman and Godyak[11].

The experiments of Godyak et al.[3-6,9] were performed with a spiral "stove-top" antenna, which covers a circular area, including antenna elements near the axis of the cylindrical chamber. The presence of non-local power deposition is more evident in experiments with antennas wrapped around the circumference of a cylinder, far from the axis. With a

curved skin layer, it is difficult to see how electrons can remain in the region of high electric field long enough to acquire high energy. Furthermore, experiments in our laboratory[12] show that the RF field can exhibit non-monotonic decay even at pressures so high that kinetic effects can be neglected. For this reason, this paper is written to clarify what can be expected from classical, collisional theory and what non-kinetic anomalies can be generated by small magnetic fields and by nonlinearities. Cylindrical geometry is emphasized to eliminate theoretical effects that can occur only in plane geometry, and realistic collision rates are considered.

II. CLASSICAL, COLLISIONAL SKIN DEPTH

A. Basic equations

Consider perturbations varying as exp(*-iwt)* in a uniform plasma with temperature KT_e, stationary ions, and density n_0 high enough that displacement current can be neglected. Maxwell's equations then read:

$$\nabla \times \mathbf{E} = iw\mathbf{B}, \qquad \nabla \times \mathbf{B} = m_0 \mathbf{j}, \tag{4}$$

and the linearized electron fluid equation is

$$-iwmn_0\mathbf{v} = -n_0 e\mathbf{E} - KT_e \tilde{\nabla} n_1 - mn_0 n\mathbf{v}, \tag{5}$$

where n_1 is the density perturbation and ν is the total electron collision frequency with ions (ν_{ei}) and with neutrals (ν_{en}). This yields the electron velocity

$$\mathbf{v} = \frac{-ie}{m(w + in)}\left(\mathbf{E} + \frac{KT_e}{e}\frac{\tilde{\nabla} n_1}{n_0}\right). \tag{6}$$

The plasma current is then

$$\mathbf{j} = -en_0\mathbf{v} = \frac{ie_0 w_p^2}{w + in}\left(\mathbf{E} + \frac{KT_e}{e}\frac{\tilde{\nabla} n_1}{n_0}\right). \tag{7}$$

For transverse waves with $\tilde{\nabla} \times \mathbf{E}$ = 0, the last term vanishes; but, in any case, it will vanish upon taking the curl of **j**, as long as n_0 is uniform. Thus we can write

$$\mathbf{j} = s\,\mathbf{E}, \qquad s = \frac{e_0 w_p^2}{n - iw}. \tag{8}$$

The curl of Ampere's Law in Eq. (1) gives

$$\nabla \times \nabla \times \mathbf{B} = m_0 \nabla \times \mathbf{j} = m_0 s\,\nabla \times \mathbf{E} = iwm_0 s\,\mathbf{B} = -\nabla^2 \mathbf{B}, \tag{9}$$

yielding a vector Helmholtz equation for the wave magnetic field:

$$\nabla^2 \mathbf{B} + iwm_0 s\,\mathbf{B} = 0. \tag{10}$$

Henceforth, n will denote n_0, and n_1 will not be used.

B. Plane geometry.

Anticipating an evanescent wave, we assume **B** to have the form $\mathbf{B} \propto \exp(-kx)$:

$$\frac{\partial^2 \mathbf{B}}{\partial x^2} = k^2 \mathbf{B} = -iwm_0 s\,\mathbf{B}\,, \tag{11}$$

so that

$$k^2 = -iwm_0 s\ . \tag{12}$$

Following Weibel[7], we define

$$e \equiv \tan^{-1}\frac{n}{w}\,, \qquad d \equiv n/w\,, \quad \text{so that} \quad d = \tan e\,. \tag{13}$$

so that k^2 can be written

$$k^2 = \left(\frac{-iwm_0 e_0 w_p^2}{n - iw}\right) = \frac{w_p^2/c^2}{1+id} = \frac{w_p^2/c^2}{(1+d^2)^{1/2}}\,e^{-ie}\,, \tag{14}$$

Re(k) is then:

$$\mathrm{Re}(k) = \cos(\tfrac{1}{2}e)/d_0\ , \qquad d_0 \equiv d_c(1+d^2)^{1/4}\,, \tag{15}$$

The collisional skin depth d_s is given by

$$d_s = 1/\mathrm{Re}(k) = d_0 \sec(e/2)\,. \tag{16}$$

Expressing e in terms of d, one obtains

$$d_s = d_c\left[\frac{2(1+d^2)}{1+(1+d^2)^{1/2}}\right]^{1/2}\,. \tag{17}$$

Note that ε is always between 0 and $\pi/2$ as ν/ω varies between 0 and ∞. For large ν/ω, $\varepsilon/2$ is always near 45°, and the real and imaginary parts of δ are nearly equal, as is the case in many high-density plasma sources. This skin depth applies to all components of **B** and depends on KT_e only through the collision term.

C. Effect of collisions.

In the calculations the collision frequencies ν_{ei} and ν_{en} as functions of T_e were fitted to polynomials using Spitzer resistivity[13] for ν_{ei} and well-known momentum-transfer cross sections[14], averaged over a Maxwellian, for ν_{en}. In practical units, we have

$$n_{en}(\mathrm{MHz}) = F_n(T_e)\,p(\mathrm{mTorr}), \qquad n_{ei}(\mathrm{MHz}) \propto n_0 T_e^{-3/2} = F_i(T_e)\,n_{11}(10^{11}\,\mathrm{cm}^3)\,, \tag{18}$$

where p is the pressure in mTorr, T_e the electron temperature in eV, and n_{11} the plasma density in units of 10^{11} cm^{-3}. The functions F_n and F_i for argon are shown in Fig. 1. The fitting curves are the functions

$$\begin{aligned} F_n(x) &= .0022 + 0.164x + 0.590x^2 - 0.114x^3 + .0067x^4 \\ F_i(x) &= 3.48T_e^{-3/2} \end{aligned} \tag{19}$$

The boundary where $n / w = 1$ is shown in Fig. 2 for various densities, pressures, and RF frequencies. It is seen that electron-neutral collisions dominate in the $10^{11\text{-}12}$ cm^{-3} region, where

the curves are horizontal, and that at argon pressures of order 10 mTorr the skin depth is collisionless at 13.56 MHz but collisional at 2 MHz.

The normal skin depth is increased by collisions, particularly at low frequencies, but it is still small compared with typical ICP radii (>15 cm). This is shown in Fig. 3, where d_s is plotted against density for various argon pressures. Even at the low frequency of 2 MHz and a low density of 10^{11} cm^{-3}, more than 10 mTorr is required for the RF field to penetrate far into the plasma. Note also that the curves follow the density scaling of d_c [Eq. (3)] up to $n \approx 10^{12\text{-}13}$ cm^{-3}, where d_s encounters a lower limit due to electron-ion collisions. The effect of collisions on d_s is also evident in Fig. 4, where d_s is plotted against p for various values of T_e. Since d_c does not depend on T_e, the variation with T_e is entirely due to collisional effects. These dependences have been shown previously by other workers[15], but without explicit calculation of the collision rates.

D. Cylindrical geometry.

Consider an infinite cylinder of radius a with a uniform antenna surface current at $r = a$. The RF field then varies only in the r direction, and $B_z\hat{\mathbf{z}}$ and $\mathbf{j}_\theta\hat{\theta}$ are the only components of **B** and **j**. Eq. (10) then can be written

$$\frac{\partial^2 B_z}{\partial r^2} + \frac{1}{r}\frac{\partial B_z}{\partial r} - k^2 B_z = 0\,, \tag{20}$$

where k is given by Eq. (14):

$$k = e^{-i\varepsilon/2}/d_0 \tag{21}$$

The relevant solution of Eq. (20) is a zero-order Bessel function of complex argument:

$$B(r) = AI_0(kr) = AJ_0(ikr)\,, \tag{22}$$

where the subscript z has been suppressed. When d is small, k reduces to $1/d_c$ or $1/d_0$, and $I_0(kr)$ represents the usual exponential decay modified by cylindrical geometry. However, in many cases of interest d is large, and $\varepsilon/2$ is nearly 45°, so that the real and imaginary parts of k are comparable. We can then consider B_z as an evanescent wave with a phase shift (I_0) or as a strongly damped propagating wave (J_0). The nature of the solution is best illustrated by the method of Joye and Schneider[2], which makes use of the familiar diagram[16] of the complex function $J_0(z)$. Consider $B(r)$ to be a J_0 function normalized to 1 on the axis. Defining

$$\rho \equiv r/d_0\,, \tag{23}$$

we have

$$B(r) = J_0(ikr) = J_0(i\rho e^{-i\varepsilon/2}) = J_0(\rho e^{i(\pi-\varepsilon)/2}) \equiv J_0(x+iy)\,. \tag{24}$$

The argument of J_0 has a magnitude r/δ_0 and an angle $\alpha = (\pi - \varepsilon)/2$, which depends only on ν/ω. This angle varies from $\pi/2$ at $\varepsilon = 0$ ($\nu = 0$) to $\pi/4$ at $\varepsilon = \pi/2$ ($\nu \to \infty$). The function $J_0(x + iy)$ is shown in the modified Joye-Schneider diagram of Fig. 5, in which the solid lines are contours of constant $|B|$, and the dotted lines its phase ϕ, defined by

$$B(r) = |B(r)|\exp[i\phi(r)]\,. \tag{25}$$

Since ¼π < α < ½π, the accessible region is that to the left of the heavy line of slope 1, representing the case $\nu \to \infty$. The region to the right can be reached only in underdense plasmas, where $\omega > \omega_p$ and the ω^2 term in Eq. (1) has to be retained, changing the sign of k^2. Measurements of $B(r)$ should lie on a straight line, as shown by the hypothetical points in Fig. 5. The slope of this line is uniquely determined by ν/ω, regardless of the collision mechanism. Once ν/ω is known, experimental points should be found to extend from the origin to $r = a/\delta_0$. A line along the y axis represents evanescent waves decaying quasi-exponentially from the boundary and described by $I_0(y)$ in the absence of collisions. A line along the x axis represents undamped propagating waves given by $J_0(x)$; for example, microwaves injected symmetrically from the wall. Damped waves would follow lines with an angle $\alpha < 45°$.

Figure 5 provides a convenient way to distinguish between normal and abnormal skin depths. Radial profiles of wave amplitude can deviate from a straight line in the presence of experimental imperfections, such as nonuniform density profile; but excursions into the forbidden region usually indicate abnormality. Henceforth, skin depths will be called "normal" when they follow classical linear electromagnetic theory without DC magnetic fields, and "abnormal" when they deviate from the predicted behavior because of nonlinear forces, stray magnetic fields, fast electrons, or other effects. By convention, the term *anomalous skin depth* will refer to kinetic modifications; thus, *anomalous* is a sub-class of *abnormal*.

Examples of field penetration into cylindrical plasmas are given in Figs. 6-10. Since d varies from small to large, the integral representation, not the asymptotic expansion, of $I_0(z)$ was used in the computations:

$$I_0(x+iy) = \frac{1}{p}\int_0^p e^{\pm x\cos q}\cos(y\cos q)\,dq + \frac{i}{p}\int_0^p e^{\pm x\cos q}\sin(y\cos q)\,dq\ .$$

Fig. 6 shows radial profiles of $|B_z|$ as n is varied from 10^{10} cm^{-3} to 10^{13} cm^{-3}, so that d_c varies by a factor of 30. Only at the lowest density does d_s / a approach unity for a = 15 cm. More importantly, the field always decays monotonically from the wall, irrespective of any reflections from the other side of the chamber. This fact can be gleaned from Fig. 5, where bounding line for the normal region is tangent to the $|J_0|$ contour at the separatrix. Enhanced penetration due to collisions is shown in Fig. 7, where the field profile is shown as a function of the neutral argon pressure for the low frequency of 2 MHz. Since collisions cause k to have a real part, the damped oscillation also propagates, with a phase variation shown in Fig. 8. Note that the phase velocity at first decreases with increasing pressure, and then increases as ν / ω surpasses unity. In Fig. 9 the radial profiles of RF magnitude and phase are compared for cylindrical and plane plasmas. There is little difference with the parameters chosen.

Though the time-averaged magnitude of B_z never reaches zero in a cylinder, its instantaneous radial profile can have a zero-crossing when k has an imaginary part due to collisions. This is illustrated in Fig. 10, computed for a highly collisional case (d = 8) in a small cylinder to emphasize this effect. Also shown is the radial profile of j_θ, which is the derivative of B_z. Both sets of curves are normalized to 1 at t = 0 and $r = a$.

III. DC MAGNETIC FIELDS

The effect of adding a small DC magnetic field parallel to the axis is subtle and almost counter-intuitive. The disruption of the shielding electron current does not greatly increase the skin depth as one would expect; electron flow in the previously ignorable z direc-

tion has to be taken into account. In this section we describe the physical mechanisms responsible for this effect and give the two-dimensional treatment necessary to compute the skin depth correctly.

Shielding of the field E_θ applied by the antenna is caused by the induced azimuthal electron currents in the plasma. When a magnetic field $\mathbf{B}_0 = B_0\hat{\mathbf{z}}$ parallel to the axis is applied, one would expect that these currents would be disrupted when the electron Larmor radii r_L become smaller than the plasma radius a. The skin depth would then increase until it reaches c/Ω_p when the ions would do the shielding, where Ω_p is the ion plasma frequency. However, the effect is complicated and requires more than a one-dimensional analysis. Previous treatments of the magnetized case[15] have simply added the B_0 terms to the plasma dielectric tensor or have concerned purely collisionless and normally unobservable effects such as resonances between the Larmor radius r_L and the tube radius. Though numerical studies[17,18] have alluded to the effects of B_0 described below, the operative physical mechanisms are not obvious.

As a baseline, we first consider the one-dimensional case of a cylinder in which $\nabla_r = \nabla_\theta = 0$. Since the infinitely long antenna has no current in the z direction, there will be no induced field in the z direction: $E_z = 0$. The linear electron equation now reads

$$m\partial\mathbf{v}/\partial t = -e(\mathbf{E} + \mathbf{v}\times\mathbf{B}_0) - mn\,\mathbf{v}\,. \tag{26}$$

Assuming $\mathbf{E} \propto \exp(-iwt)$ and solving for $\mathbf{v}$, we have

$$v_r = -\frac{ie}{m\hat{w}}\frac{E_r - i(w_c/\hat{w})E_q}{1-w_c^2/\hat{w}^2}, \qquad v_q = -\frac{ie}{m\hat{w}}\frac{E_q + i(w_c/\hat{w})E_r}{1-w_c^2/\hat{w}^2}, \tag{27}$$

where

$$w_c \equiv eB_0/m, \qquad \hat{w} \equiv w + in\,, \qquad w_p \equiv (ne^2/e_0 m)^{1/2}, \qquad k_0 = w/c\,. \tag{28}$$

The relevant components of the current $\mathbf{j} = -ne\mathbf{v}$ can then be written

$$j_r = \frac{ie_0 w_p^2 E_r}{\hat{w}(1-w_c^2/\hat{w}^2)}, \qquad j_q = \frac{ie_0 w_p^2 E_q}{\hat{w}(1-w_c^2/\hat{w}^2)}\,. \tag{29}$$

Using this in Maxwell's equations

$$\nabla\times\mathbf{E} = iw\mathbf{B}, \qquad \nabla\times\mathbf{B} = m_0(\mathbf{j} - iwe_0\mathbf{E})\,, \tag{30}$$

we obtain

$$\nabla^2\mathbf{B} + k_0^2\mathbf{B} + m_0\nabla\times\mathbf{j} = 0. \tag{31}$$

By symmetry, $\mathbf{B}$ can have only one component B_z, and $\mathbf{j}$ and $\mathbf{E}$ have only q components. Hence,

$$\nabla\times\mathbf{j} = \hat{\mathbf{z}}\frac{1}{r}\frac{\partial}{\partial r}(rj_q)\,, \tag{32}$$

$$m_0(\nabla\times\mathbf{j})_z = \frac{iw_p^2}{c^2}\frac{(\nabla\times\mathbf{E})_z}{\hat{w}(1-w_c^2/\hat{w}^2)} = -\frac{w_p^2}{c^2}\frac{w}{\hat{w}}\frac{B_z}{1-w_c^2/\hat{w}^2}\,. \tag{33}$$

Equation (31) then becomes

$$\nabla^2 B_z + k_0^2 B_z - k_s^2 \frac{w/\hat{w}}{1 - w_c^2/\hat{w}^2} B_z = 0 . \tag{34}$$

The k_0^2 term can safely be neglected, and we have Bessel's equation (20) with the solution

$$B_z = A\mathrm{I}_0(Tr) , \tag{35}$$

where

$$T = k_s \left[(1+id) \left(1 - \frac{w_c^2/w^2}{(1+id)^2} \right) \right]^{-1/2} , \tag{36}$$

with d as in Eq. (13). Defining

$$g \equiv w_c / w , \tag{37}$$

we can write T as $T = |T|\exp(iy)$. Without assuming either d or g to be large or small, we find

$$\begin{aligned} |T| &= k_s (1+d^2)^{1/2} \left[(1+d^2-g^2)^2 + d^2(1+d^2+g^2)^2 \right]^{-1/4} \\ y &= -\frac{1}{2} \tan^{-1} \left[\frac{d(1+d^2+g^2)}{1+d^2-g^2} \right] , \end{aligned} \tag{38}$$

which reduces to Eq. (14) when $g = 0$. An example of this solution is shown in Figs. 11 and 12 for a case in which $d = 0.23$ and $g = 1$ at $B_0 = 5$G. Note that the increase in skin depth is not monotonic below this field because of the effect of collisions. This effect is even more evident in the phase velocities seen in Fig. 12.

Although this simple treatment for $E_r = E_z = 0$ gives reasonable results, the results are spurious. This physical situation cannot occur in a cylinder for the following reason. The magnetic field bends the orbits of the orbits of the electrons driven by the E_θ field, causing them to move in the r direction. In cylindrical geometry, this necessarily causes a buildup of negative charge in the interior, leading to a radial field E_r. Thus, the problem requires treating more than one component of both **B** and **E**. The solution is a linear superposition of two modes, variously called the TE and TM modes in electromagnetic theory, ordinary and extraordinary waves in plasma theory, and helicon (H) and Trivelpiece-Gould (TG) modes in helicon theory. The theoretical framework for the general case has already been given in the context of helicon waves[19] and can easily be extended to the $B_0 = 0$ case of ICPs. The governing equation for the wave magnetic field **B** is[19]:

$$\nabla \times \nabla \times \mathbf{B} - g k_z \nabla \times \mathbf{B} + k_s^2 \mathbf{B} = 0 . \tag{39}$$

The general solution is $\mathbf{B} = \mathbf{B}_1 + \mathbf{B}_2$, where $\mathbf{B}_j$ satisfies $\nabla^2 \mathbf{B}_j + b_j^2 \mathbf{B}_j = 0$, and b_j are the roots of the quadratic

$$b_{1,2} = \frac{g k_z}{2} \mp i k_s \left(1 - \frac{g^2 k_z^2}{4 k_s^2} \right)^{1/2} , \tag{40}$$

and we have assumed perturbations of the form $\mathbf{B}(r)\exp[i(mq + k_z z - wt)$. For clarity we take g to be real here, as defined by Eq. (37); but collisions will be included in the computations by replacing w by $w + in$. When $g = 0$ ($B_0 = 0$), both roots yield the classical skin depth $1/k_s$. However, contrary to the TE results of Fig. 11, the magnetic field has no effect on the skin depth if $k_z = 0$. The physical reason for this is shown in Fig. 13. At the RF phase in which the antenna current is in the $+q$ direction, as shown, the induced field $\mathbf{E}_\theta$ is in the $-q$ direction, driving the electrons in the $+q$ direction. The Lorentz force $-e\mathbf{v} \times \mathbf{B}_0$ is then in the $-r$ direction, creating a negative charge accumulation because of the smaller volume at smaller r. The resulting electrostatic field $\mathbf{E}_2$ is in the $-r$ direction, causing an electron drift $\mathbf{E}_2 \times \mathbf{B}_0$ in the original $+q$ direction. The field $\mathbf{E}_2$ builds up until the force $-eE_{2r}$ on the electrons cancels the Lorentz force due to $\mathbf{B}_0$. The original shielding current j_θ is then restored, and $\mathbf{B}_0$ no longer affects it. If k_z does not vanish, however, the charge accumulation can be dissipated by electron flow along $\mathbf{B}_0$, and j_θ will indeed be decreased, permitting deeper penetration of the RF field.

For $m = 0$, the radial profiles of B_r, B_θ, and B_z in a uniform plasma are given by[19]

$$B_r, B_q \propto J_1(Tr), \quad B_z \propto J_0(Tr) , \tag{41}$$

where

$$T = (b^2 - k_z^2)^{1/2} . \tag{42}$$

Examples of B_z profiles are shown in Figs. 14-16, with collisions taken into account as in Sec. IIB. In addition, ion collisions and displacement current have also been included by exact evaluation of the coefficients in Eq. (39) from the plasma dielectric tensor[20]. Figure 14 shows that for $k_z = 0$ the magnetic field has little effect on the skin depth up to the order of 1kG, the only effect coming from the collisional part of the small added terms. Figure 15 shows that the effect of k_z is to reduce the skin depth when $B_0 = 0$. We next show the effect of k_z at a finite DC field of 100 G. There are now two modes, the TG mode, corresponding to the + sign in Eq. (40), and the H mode, corresponding to the – sign. Figure 16 shows that the effect of k_z on the TG mode is not monotonic, but in any case is not large. On the other hand, Fig. 17 shows that the H mode becomes a propagating mode and reaches deeply into the plasma when $k_z > k_{min}$, where

$$k_{min} \equiv 2k_s / g . \tag{43}$$

As can be seen from Eq. (40), both roots become real for $k_z > k_{min}$, but the TG mode is heavily damped by collisions. It is clear that the k_z-spectrum of the oscillations is critical in determining the skin depth, and the two modes must be added together with the proper amplitude ratio as determined by the boundary conditions.

The exact solution can be computed using the HELIC code developed by Arnush[21] for helicon waves. Examples of such computations are shown in Fig. 18 for magnetic fields of 1 G to 1000 G for an antenna consisting of a single loop at $z = 0$. These curves are the result of summing over the H and TG modes with the proper phases and amplitudes, and summing over the k-spectrum of the oscillations excited by the antenna. The cylinder is infinite with no endplates, and the density is assumed to be uniform. These conditions are assumed in order to compare with the previous results, although the code is equipped to handle the more general case. It is seen in Fig. 18 that B_0 indeed increases the skin depth, but not as much as one might have expected. Though the $|B_z|$ profiles are similar, the phase velocities vary greatly as B_0 is changed. This is because the k-spectrum, shown in Fig. 19 on a log-log

scale, depends sensitively on B_0. The effect of changing the k-spectrum is illustrated in Figs. 20 and 21, which show the same calculations as in Figs. 18 and 19, but for an m = 1 half-wavelength helical antenna 20 cm long. Since in this case the B_z component is not the dominant one in the midplane of the antenna, the magnitude of the total **B** is plotted here. The effect of wave propagation is evident in the non-exponential wave profiles, which do not even increase monotonically with B_0. In summary, the addition of a small DC field to skin depth calculations is non-trivial and requires an understanding of the underlying physical mechanisms.

IV. NONLINEAR EFFECTS

When the RF magnetic field **B** is large enough to affect the electrons' motion, nonlinear terms in the equation of motion have to be retained. In the frame moving with an electron, its equation of motion is

$$m\frac{d\mathbf{v}}{dt} = -e(\mathbf{E} + \mathbf{v}\times\mathbf{B}) - mn\,\mathbf{v}\,, \tag{44}$$

where **E** and **B** are evaluated at the instantaneous position of the electron. In the equivalent fluid formulation, **E** and **B** are evaluated in the laboratory frame, and the convective derivative has to be added so that $d/dt = \partial/\partial t + \mathbf{v}\cdot\nabla\mathbf{v}$. Since $\mathbf{v}\cdot\nabla\mathbf{v}$ and $\mathbf{v}\times\mathbf{B}$ partially cancel each other, it is insufficient to consider the nonlinear Lorentz force $\mathbf{v}\times\mathbf{B}$ alone, as some authors have done[22]. Furthermore, since **v** and **B** are phase-related so as to make the electrons oscillate with a figure-8 motion, **B** cannot be averaged and treated as an effective DC magnetic field[23]. These nonlinear effects are best treated as a nonlinear force $\mathbf{F}_{NL}$, called the ponderomotive force in laser-plasma interactions, which causes a drift of the figure-8 orbits when there is a gradient in the field strength. Kinetic effects in collisionless plasmas can also be nonlinear[24], but these are irrelevant to high-density plasmas. The ponderomotive force can cause nonlinear effects that have already been seen, such as displacement of the plasma away from the wall[25], generation of a second harmonic field at $2w$[26], and changes in the electron energy distribution[27]. Here we derive other ponderomotive force effects not considered before.

Following Schmidt[28], we solve Eq. (44) order by order. In lowest order, let the local RF field be

$$\mathbf{E}^{(1)} = \mathbf{E}_s \cos wt\,, \tag{45}$$

where $\mathbf{E}_s$ denotes the spatial part. Neglecting the nonlinear terms in this order and integrating twice, we obtain

$$\begin{aligned} m d\mathbf{v}^{(1)}/dt &= -e\mathbf{E}_s\cos wt - mn\,\mathbf{v} \\ \mathbf{v}^{(1)} &= -\frac{e}{mw}\mathbf{E}_s(1+d^2)^{-1}(\sin wt + d\cos wt) = (d/dt)\mathbf{dr}^{(1)} \\ \mathbf{dr}^{(1)} &= \frac{e}{mw^2}\mathbf{E}_s(1+d^2)^{-1}(\cos wt - d\sin wt), \end{aligned} \tag{46}$$

where $d = n/w$ and $\mathbf{dr}^{(1)}$ is the excursion of the electron. Faraday's Law gives

$$-d\mathbf{B}^{(1)}/dt = \nabla\times\mathbf{E}^{(1)} = \nabla\times\mathbf{E}_s\cos wt$$
$$\mathbf{B}^{(1)} = -\frac{1}{w}\nabla\times\mathbf{E}_s\sin wt. \tag{47}$$

These equations are in the frame of the moving electron. Hence, in second order, **E** must be evaluated at the position $\mathbf{r}_0$ + $\mathbf{dr}^{(1)}$. The second order terms in the equation of motion are then

$$m\frac{d\mathbf{v}^{(2)}}{dt} = -e[(\mathbf{r}^{(1)}\cdot\nabla)\mathbf{E}^{(1)} + \mathbf{v}^{(1)}\times\mathbf{B}^{(1)}] - mn\,v^{(2)}. \tag{48}$$

Substituting the first-order terms from Eqs. (46) and (47), we obtain

$$\frac{d\mathbf{v}^{(2)}}{dt} + n\,\mathbf{v}^{(2)} = -\frac{e^2}{m^2w^2}\frac{1}{1+d^2}\times$$
$$\left[(\cos^2 wt - d\,\sin wt\cos wt)\hat{\mathbf{?}}_s\cdot\nabla\hat{\mathbf{?}}_s + (\sin^2 wt + d\,\sin wt\cos wt)\hat{\mathbf{?}}_s\times(\nabla\times\hat{\mathbf{?}}_s)\right]. \tag{49}$$

Using trigonometric identities and the vector identity

$$\mathbf{E}_s\times\nabla\times\mathbf{E}_s = \tfrac{1}{2}\nabla\mathbf{E}_s^2 - (\mathbf{E}_s\cdot\nabla)\mathbf{E}_s, \tag{50}$$

we combine the two vector terms to obtain

$$\frac{d\mathbf{v}^{(2)}}{dt} + n\,\mathbf{v}^{(2)} = -\frac{e^2}{m^2w^2}\frac{1}{1+d^2}[\mathbf{G}(1-\cos 2wt + d\,\sin 2wt) + \mathbf{H}(\cos 2wt - d\,\sin 2wt)], \tag{51}$$

where

$$\mathbf{G} \equiv \tfrac{1}{4}\nabla\mathbf{E}_s^2, \qquad \mathbf{H} \equiv \mathbf{E}_s\cdot\nabla\mathbf{E}_s. \tag{52}$$

The so-called ponderomotive force per unit volume is found by multiplying the right-hand side by *mn* and using the definition of w_p:

$$\mathbf{F}_{NL} = -\frac{w_p^2}{w^2}\frac{1}{1+d^2}\left[\nabla\frac{\langle e_0E_s^2\rangle}{2}(1-\cos 2wt + d\,\sin 2wt) + \mathbf{E}_s\cdot\nabla\mathbf{E}_s(\cos 2wt - d\,\sin 2wt)\right]. \tag{53}$$

The DC term is the usual ponderomotive force[29], modified by collisions. The cos2*wt* terms have been investigated extensively by Godyak et al.[26,30]. In a plane wave with intensity varying in the direction of propagation, $(\mathbf{E}_s\times\tilde{N})\mathbf{E}_s$ would vanish, since $\mathbf{E}_s$ and $\tilde{N}$ are perpendicular to each other. In our geometry of a symmetric cylinder, $\mathbf{E}_s$ is in the *q* direction and the only gradient is in the *r* direction, but $(\mathbf{E}_s\times\tilde{N})\mathbf{E}_s$ does not vanish because the unit vector $\hat{\mathbf{?}}$ varies with *q*. We then have $\mathbf{E} = E_q\hat{\mathbf{?}}$, and $(\mathbf{E}_s\cdot\nabla)\mathbf{E}_s = -\hat{\mathbf{r}}E_s^2/r$, a nonlinear centrifugal force at the second harmonic. If we neglect this term, $\mathbf{F}_{NL}$ takes the simple form

$$\mathbf{F}_{NL} = -\frac{w_p^2}{w^2}(1+d^2)^{-1}\left[\frac{e_o}{2}\nabla\left\langle\mathbf{E}_s^2\right\rangle(1-\cos 2wt + d\,\sin 2wt)\right]. \tag{54}$$

This expression agrees with that given by Piejak and Godyak[31], who predicted that the second harmonic would dominate when $d >> 1$. Indeed, squaring the $2w$ terms and averaging over time, we find the $2w$ component to be given by

$$\left\langle \mathbf{F}_{NL}^2(2w)\right\rangle^{1/2} = \left[\frac{w_p^2}{w^2}\frac{e_o}{(1+d^2)}\nabla\left\langle \tfrac{1}{2}\mathbf{E}_s^2\right\rangle\right]\frac{1}{\sqrt{2}}\left(1+d^2\right)^{1/2} = \frac{1}{\sqrt{2}}\left[\frac{w_p^2}{w^2}\frac{e_o}{(1+d^2)^{1/2}}\nabla\left\langle \tfrac{1}{2}\mathbf{E}_s^2\right\rangle\right]. \quad (55)$$

The ratio of $\langle\mathbf{F}_{2w}\rangle$ to $|\mathbf{F}_{DC}|$ is $(1+d^2)^{1/2}/\sqrt{2}$, which increases with d. Both $\mathbf{F}_{DC}$ and $\mathbf{F}_{2w}$ decrease with d, but $\mathbf{F}_{DC}$ decreases faster.

The DC force causes $\mathbf{v}^{(2)}$ to increase secularly. We can solve Eq. (51) for $\mathbf{v}^{(2)}$ by assuming $\mathbf{v}^{(2)}$ to be of the form

$$\mathbf{v}^{(2)} = \mathbf{v}_1 t + \mathbf{v}_2 \sin 2wt + \mathbf{v}_3 \cos 2wt, \quad (56)$$

and solving for $\mathbf{v}_1$, $\mathbf{v}_2$, and $\mathbf{v}_3$ by matching the time dependences. After some algebra, we obtain

$$\mathbf{v}^{(2)} = -\frac{e^2}{m^2w^2}(1+d^2)^{-1}\left[\mathbf{G}t + \frac{1}{w}\frac{d^2-2}{d^2+4}(\mathbf{G}-\mathbf{?})\sin 2wt - \frac{1}{w}\frac{3d}{d^2+4}(\mathbf{G}-\mathbf{?})\cos 2wt\right], \quad (57)$$

In cylindrical symmetry, $\mathbf{G} - \mathbf{H}$ simplifies to

$$\mathbf{G}-\mathbf{H} = \tfrac{1}{4}\nabla E_s^2 + \hat{\mathbf{r}}E_s^2/r = \hat{\mathbf{r}}(r^4E_s^2)'/4r^4, \quad (58)$$

where the prime indicates $\partial/\partial r$.

In the absence of a DC magnetic field, the only waves other than this electromagnetic wave which can propagate in a plasma are the electron plasma wave and the ion acoustic wave. The former has a frequency near w_p and cannot be directly excited by the RF. An ion wave, however, can possibly be excited, either directly by the ponderomotive force or through the stimulated Brillouin scattering instability, leading to propagation of RF energy beyond the skin depth. In second order, there are no effects at the frequency w which could lead to excitation of ion waves. To find such an effect, we have to go to third order. For simplicity, we neglect both d and $\mathbf{H}$ in this calculation. In that case, Eq. (57) simplifies to

$$\mathbf{v}^{(2)} = \frac{e^2}{m^2w^3}\frac{1}{8}\nabla E_s^2\left(2wt - \sin 2wt\right). \quad (59)$$

The third-order equation of motion is

$$\frac{d\mathbf{v}^{(3)}}{dt} = -\frac{e}{m}\left[(\mathbf{dr}^{(1)}\cdot\nabla)\mathbf{E}^{(2)} + (\mathbf{dr}^{(2)}\cdot\nabla)\mathbf{E}^{(1)}\right] + \mathbf{v}^{(1)}\times\mathbf{B}^{(2)} + \mathbf{v}^{(2)}\times\mathbf{B}^{(1)}, \quad (60)$$

where

$$\mathbf{E}^{(2)} = (\mathbf{dr}^{(1)}\cdot\nabla)\mathbf{E}^{(1)} \quad (61)$$

and

$$\frac{d\mathbf{B}^{(2)}}{dt} = -\nabla\times\mathbf{E}^{(2)}. \quad (62)$$

Both $\mathbf{E}^{(2)}$ and $\mathbf{B}^{(2)}$ vanish with the neglect of $\mathbf{E}_s\cdot\nabla\mathbf{E}_s$. Integrating Eq. (59), we find

$$\mathbf{dr}^{(2)} = \frac{e^2}{m^2 w^3}\frac{1}{8}\nabla E_s^2\left(wt^2 + \frac{1}{2w}\cos 2wt\right). \tag{63}$$

Inserting this into Eq. (60) and multiplying by *mn*, we obtain for the third-order ponderomotive force

$$\mathbf{F}_3 = -en\left(\frac{e}{mw^2}\right)^2 \frac{1}{16}\left\{\left[\mathbf{H}_2 + (2w^2t^2 + \tfrac{1}{2})\mathbf{G}_2\right]\cos wt - 4wt\mathbf{H}_2 \sin wt + (\tfrac{1}{2}\mathbf{G}_2 - \mathbf{H}_2)\cos 3wt\right\}, \tag{64}$$

where

$$\mathbf{G}_2 \equiv \left(\nabla E_s^2 \cdot \nabla\right)\mathbf{E}_s, \qquad \mathbf{H}_2 \equiv \nabla E_s^2 \times (\nabla \times \mathbf{E}_s). \tag{65}$$

In cylindrical symmetry, use of Eq. (50) yields $\mathbf{H}_2 = -\mathbf{G}_2$, and $\mathbf{G}_2$ can be written

$$\mathbf{G}_2 \equiv \left(\nabla E_s^2 \cdot \nabla\right)\mathbf{E}_s = (E_s^2)'\mathbf{E}_s' = 2(E_s')^2\mathbf{E}_s. \tag{66}$$

$\mathbf{F}_3$ then becomes

$$\mathbf{F}_3 = -\frac{en}{8}\left(\frac{e}{mw^2}\right)^2 (E_s')^2\,\mathbf{E}_s\left[(2w^2t^2 - \tfrac{1}{2})\cos wt + 4wt\sin wt + \frac{3}{2}\cos 3wt\right]. \tag{67}$$

For $wt >> 1$, the dominant term in $\mathbf{F}_3$ is

$$\mathbf{F}_3 = -\tfrac{1}{4}ne\left(\frac{eE_s'}{mw^2}\right)^2 w^2t^2\mathbf{E}_s\cos wt. \tag{68}$$

This is in the same direction as the force applied by $\mathbf{E}^{(1)}$ and therefore cannot lead to any new effects.

V. Conclusions

Classical skin depths were calculated with arbitrarily large collisionality in cylindrical geometry. It was found that non-monotonic radial profiles of $|B_z|$, as are sometimes observed, are not possible in this context. Addition of a DC magnetic field affects the skin depth in a way which is sensitive to the k_z spectrum excited by the antenna. The skin depth is greatly increased only when B_0 is large enough for helicon waves to propagate. The nonlinear ponderomotive force was calculated with arbitrary collisionality. The normal DC ponderomotive force was recovered, as well as the well-known second harmonic force. Collisions were found to weaken the second harmonic. The third-order ponderomotive force was calculated for the collisionless case. A secularly increasing force at the fundamental frequency was found, but this is in the q direction, not the r direction, and is in the same direction as that of the applied RF field. Non-monotonic behavior of $|B_z|(r)$ cannot be explained by collisions, by geometry, by DC magnetic fields, or by nonlinear effects induced by the wave's magnetic field.

VI. Acknowledgments

This work was supported by Applied Materials, Inc., the University of California SMART program, and the Semiconductor Research Corporation. We thank R. Piejak for his useful comments.

FIGURE CAPTIONS

Fig. 1. Curves used to fit electron-ion and electron-neutral collision frequencies as functions of electron temperature.

Fig. 2. Dividing line between high and low collisionality for various RF frequencies.

Fig. 3. Classical skin depth vs. density at various neutral pressures.

Fig. 4. Effect of argon pressure on skin depth at various electron temperatures.

Fig. 5. Contours of constant amplitude of the function $J_0(x + iy)$ (solid lines) and of its phase (in degrees, dotted lines). The points are hypothetical measurements of the radial profile of wave amplitude, normalized to unity at $r = 0$. The angle α depends only on ν / ω, and has been drawn here for $\nu / \omega = 1$.The diagonal line is the boundary for "normal" skin depth measurements in a collisional plasma.

Fig. 6. Field penetration into a cylindrical plasma of various densities.

Fig. 7. Field penetration into a cylindrical plasma at various pressures.

Fig. 8. Variation of phase velocity with pressure. Note that the variation is not monotonic.

Fig. 9. Effect of cylindrical geometry on field profiles.

Fig. 10. Instantaneous radial profiles of B_z (left) and J_θ (right) in a case with large ν / ω and d_s / a. The curves are flipped during the second half-cycle. The shaded line is the envelope of the magnitude of B_z.

Fig. 11. Effect of an applied DC magnetic field on penetration of a 13.56-MHz RF field into a 15-cm radius cylindrical plasma in the TE approximation. Electron collisions are computed for $T_e = 3$ eV, $n = 5 \times 10^{11}$ cm^{-3}, and $p = 5$ mTorr of argon; ion collisions are neglected.

Fig. 12. Relative phase of the RF signal for the case of Fig. 11.

Fig. 13. Physical mechanism of RF penetration across a DC magnetic field.

Fig. 14. Computed field magnitude profiles for $k_z = 0$ at various magnetic fields B_0. Conditions are: $f = 13.56$MHz, $T_e = 3$eV, $p = 5$mT, $n = 5 \times 10^{11}$ cm^{-3}, $a = 15$cm.

Fig. 15. Computed field magnitude profiles for $B_0 = 0$ and various values of k_z . Conditions are the same as in Fig. 14.

Fig. 16. Computed field magnitude profiles of the TG mode for $B_0 = 100$ G and various values of k_z . Conditions are the same as in Fig. 14. The variation is not monotonic; the curves appear in the same order as in the legend.

Fig. 17. Computed field magnitude profiles of the helicon mode for $B_0 = 100$ G and various values of k_z . Conditions are the same as in Fig. 14.

Fig. 18. Exact calculations of field profiles at various magnetic fields using the HELIC code. Conditions are as in Fig. 14.

Fig. 19. The spectrum $P(k_z)$ of power deposited per unit k corresponding to the curves on Fig. 17. Logarithmic scales are used because the coupling efficiency is two orders of magnitude lower at low B_0 fields corresponding to ICP operation. The peaks at high fields correspond to eigenmodes of the coupled helicon-TG waves.

Fig. 20. Same as Fig. 18 except that the antenna is a half-wavelength helix with $m = 1$ symmetry, and the total $|\mathbf{B}|$ is plotted rather than $|B_z|$.

Fig. 21. The spectrum of waves in the plasma producing the field profiles of Fig. 20 at various magnetic fields.

REFERENCES

[1] R.A. Demirkhanov, I.Ya. Kadysh, and Yu. S. Khodyrev, Soviet Phys. JETP **19**, 791 (1964).

[2] B. Joye and H. Schneider, Helv. Phys. Acta **51**, 804 (1978).

[3] V.A. Godyak and V.I. Kolobov, Phys. Rev. Lett. **79**, 4589 (1997).

[4] V.A. Godyak and R.B. Piejak, J. Appl. Phys. **82**, 5944 (1997).

[5] R. Piejak, V.A. Godyak, and B. Alexandrovich, J. Appl. Phys. **81**, 3416 (1997).

[6] V.A. Godyak, in *Electron Kinetics and Applications of Glow Discharges*, ed. by U. Kortshagen and L. Tsendin (Plenum, New York, 1998).

[7] E.S. Weibel, Phys. Fluids **10**, 741 (1967).

[8] Yu. S. Sayasov, Helv. Phys. Acta **52** 288 (1979).

[9] V.A. Godyak, R.B. Piejak, B.M. Alexandrovich, and V.I. Kolobov, Phys. Rev. Lett. **80**, 3264 (1998).

[10] V.I. Kolobov and D.J. Economou, Plasma Sources Sci. Technol. **6**, R1 (1997).

[11] M.A. Lieberman and V.A. Godyak, IEEE Trans. Plasma Sci. **26**, 955 (1998).

[12] J.D. Evans, F.F. Chen, and D. Arnush, *Investigation of Electromagnetic Field Penetration in ICP and Weakly-Magnetized ICP Discharges*, Proc. ICPP-2000, Quebec, Canada (October 23-27, 2000), Paper GP1.017.

[13] D.L. Book, in *A Physicist's Desk Reference*, H.L. Anderson, ed. (Amer. Inst. Phys., New York, 1989), p. 281.

[14] W.L. Morgan, www.kinema.com.

[15] S. Shinohara and Y. Kawai, Jpn. J. Appl. Phys. **35**, L725 (1996).

[16] E. Jahnke and F. Emde, Tables of Functions, 4th ed. (Dover, New York, 1945), p. 127.

[17] R.H. Cohen and T.D. Rognlien, Phys. Plasmas **3**, 1839 (1996).

[18] R.H. Cohen and T.D. Rognlien, Plasma Sources Sci. Technol. **5** 442 (1996).

[19] F.F. Chen and D. Arnush, Phys. Plasmas **4**, 3411 (1997); UCLA PPG-1562 (Aug 1996).

[20] D. Arnush and F.F. Chen, Phys. Plasmas **5**, 1239 (1998), Appendix.

[21] D. Arnush, Phys. Plasmas **7**, 3042 (2000).

[22] A.I. Smolyakov and I. Khabibrakhmanov, Phys. Rev. Lett. **81**, 4871 (1998).

[23] M. Tuszewski, Phys. Rev. Lett. **77**, 1286 (1996).

[24] Yu.M. Aliev, I.D. Kaganovich, and H. Schlüter, Phys. Plasmas **4**, 2413 (1997).

[25] G. Tynan and S.M. Yun, to be published.

[26] V.A. Godyak, R.B. Piejak, and B.M. Alexandrovich, Phys. Rev. Lett. **83**, 1610 (1999).

[27] C. Chung, S-H. Seo, and H-Y. Chang, Phys. Plasmas **7,** 3584 (2000).

[28] G. Schmidt, *Physics of High Temperature Plasmas*, 2nd ed. (Academic, New York, 1979), p. 47 *ff*.

[29] F.F. Chen, *Intro. to Plasma Physics and Controlled Fusion*, 2nd ed., Vol. 1 (Plenum, New York, 1984), Sec. 8.4.

[30] V. A. Godyak, R. B. Piejak and B. M. Alexandrovich, Phys. Plasmas **6**, 1804 (1999).

[31] R.B. Piejak and V.A. Godyak, Appl. Phys. Lett. **76**, 2188 (2000).

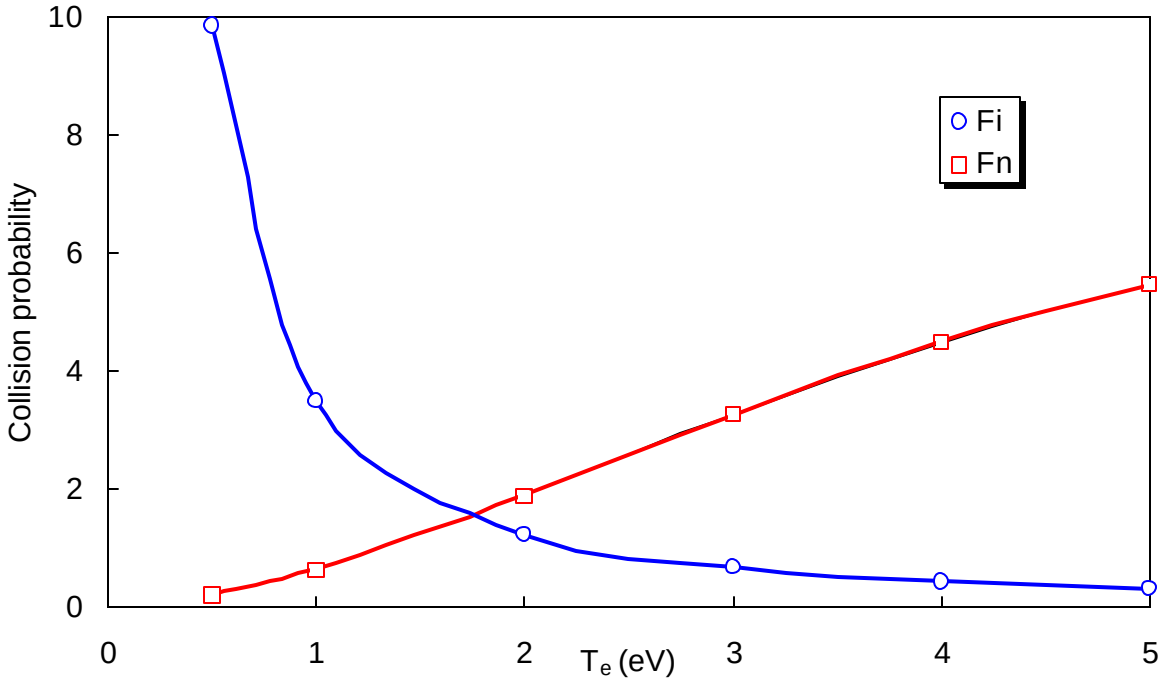

Fig. 1. Curves used to fit electron-ion and electron-neutral collision frequencies as functions of electron temperature.

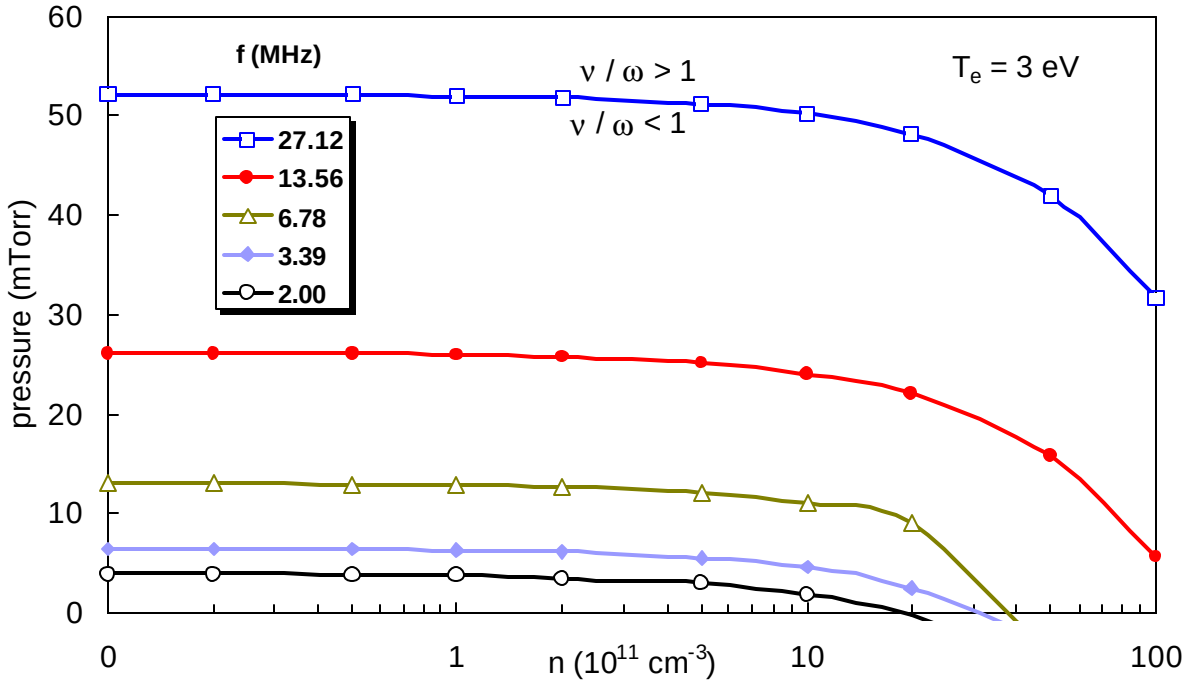

Fig. 2. Dividing line between high and low collisionality for various RF frequencies.

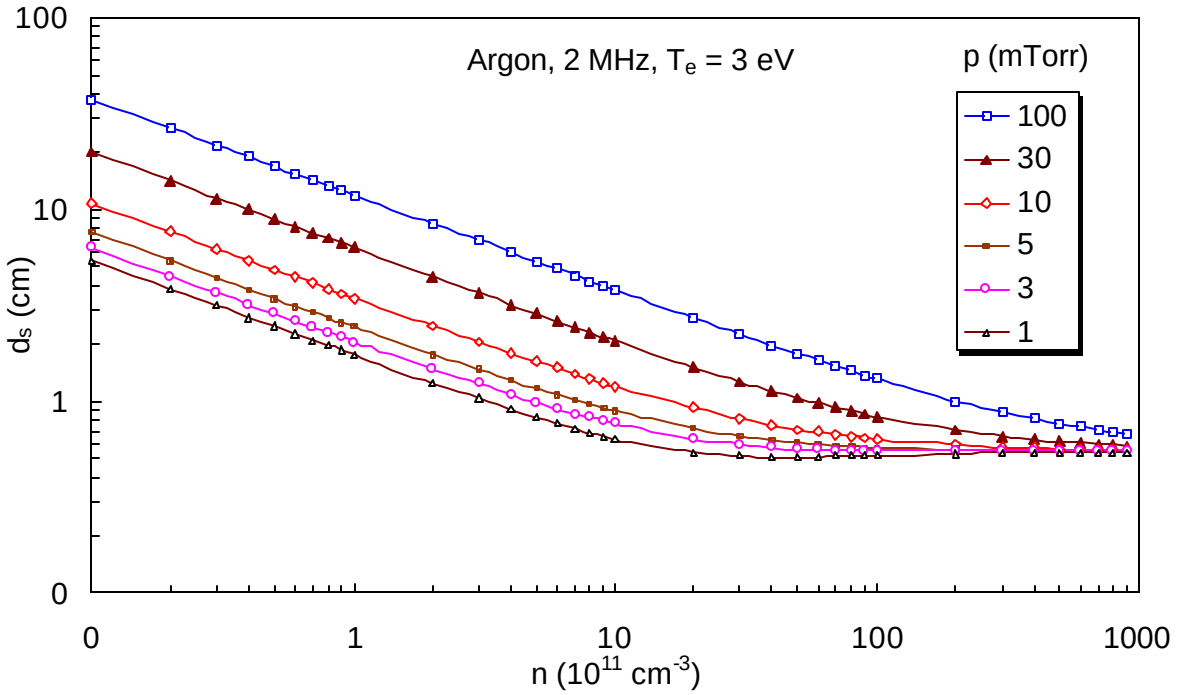

Fig. 3. Classical skin depth vs. density at various neutral pressures.

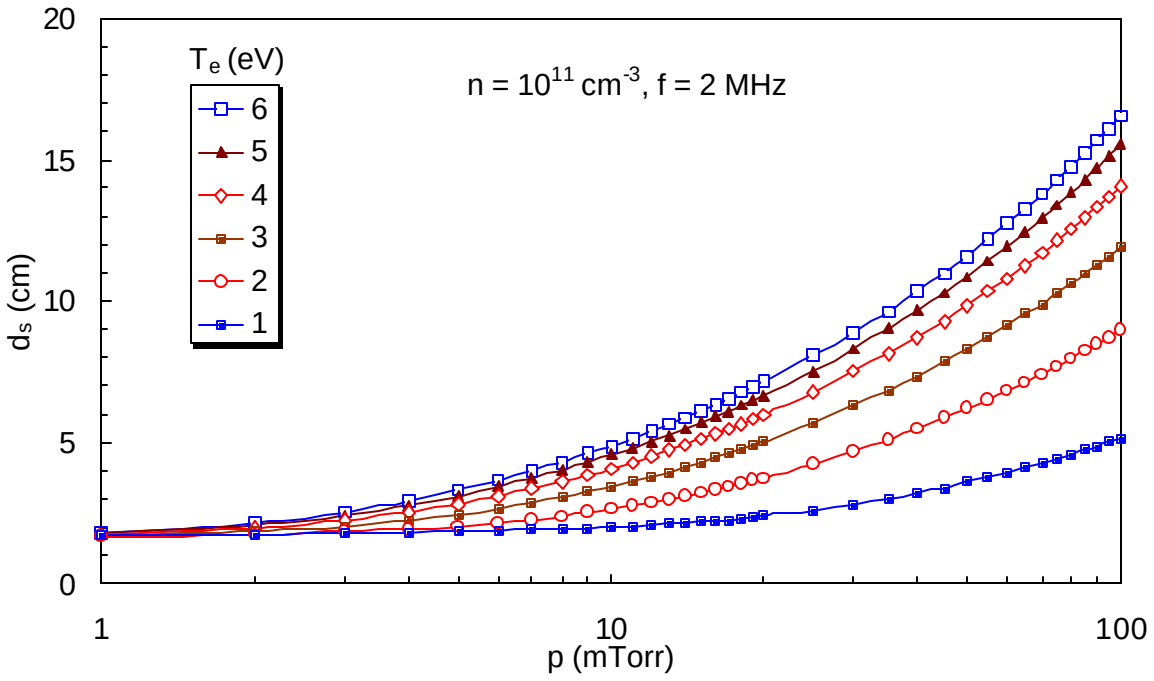

Fig. 4. Effect of argon pressure on skin depth at various electron temperatures.

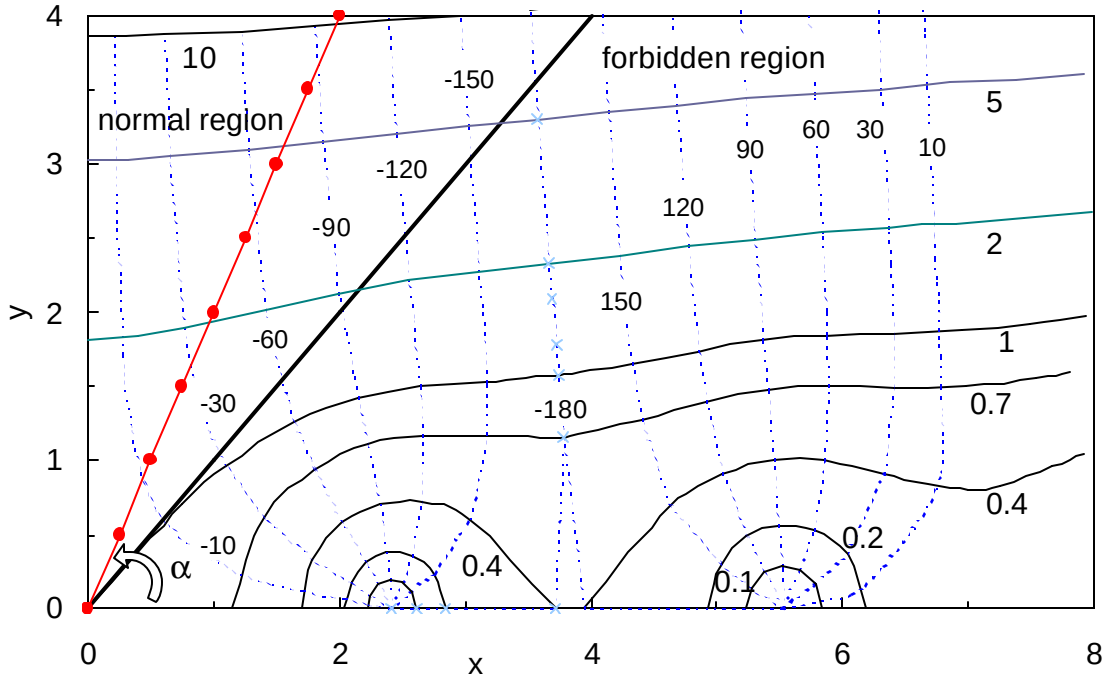

Fig. 5. Contours of constant amplitude of the function $J_0(x + iy)$ (solid lines) and of its phase (in degrees, dotted lines). The points are hypothetical measurements of the radial profile of wave amplitude, normalized to unity at $r = 0$. The angle α depends only on ν / ω, and has been drawn here for $\nu / \omega = 1$.The diagonal line is the boundary for "normal" skin depth measurements in a collisional plasma.

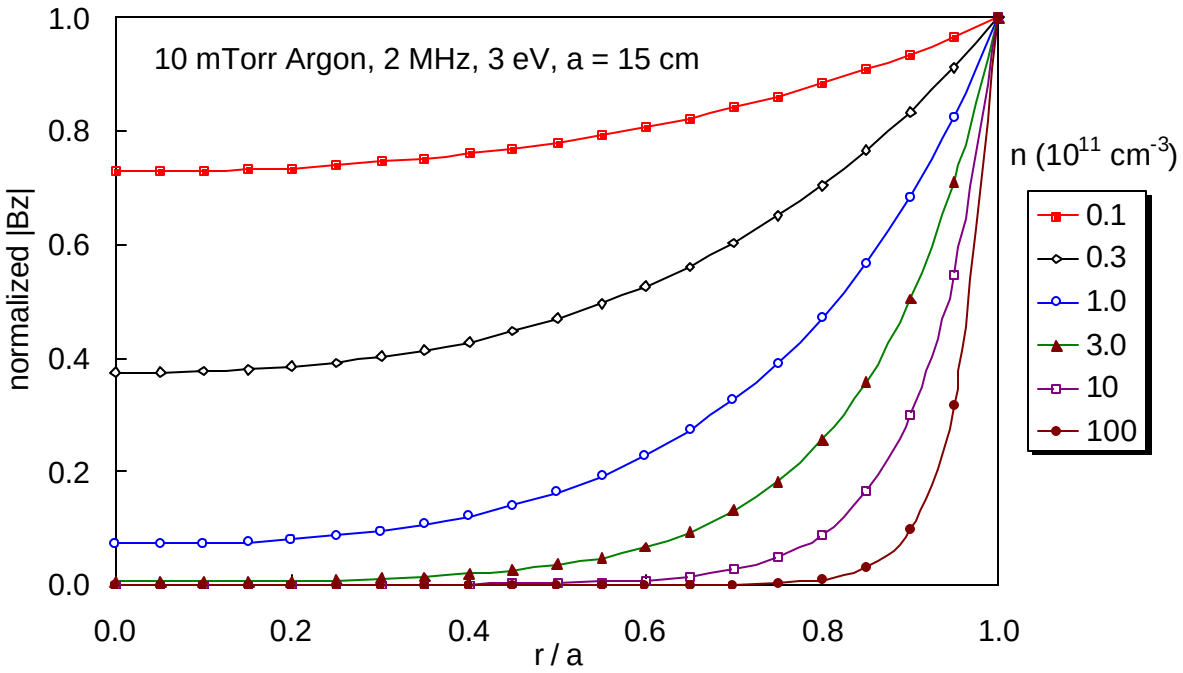

Fig. 6. Field penetration into a cylindrical plasma of various densities.

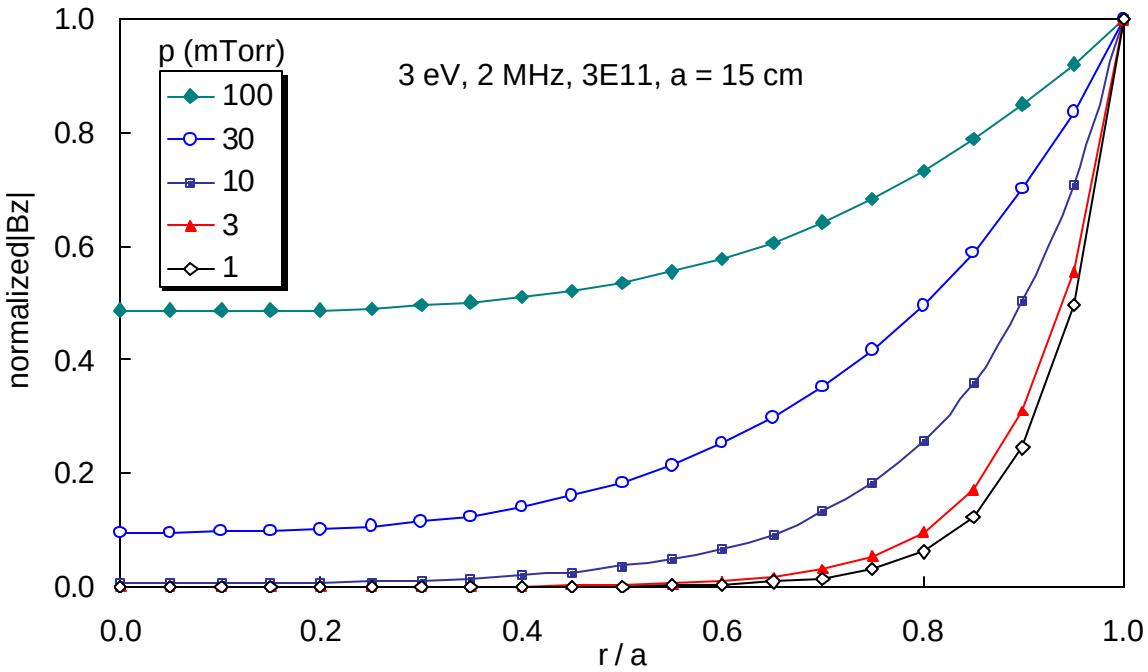

Fig. 7. Field penetration into a cylindrical plasma at various pressures.

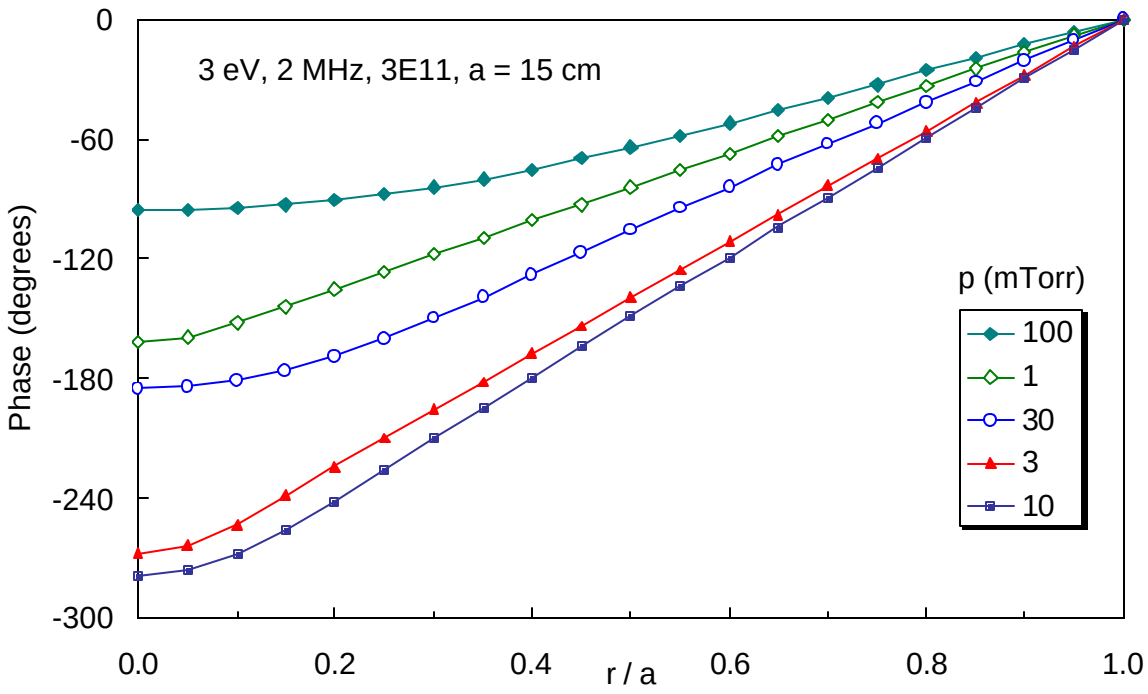

Fig. 8. Variation of phase velocity with pressure. Note that the variation is not monotonic.

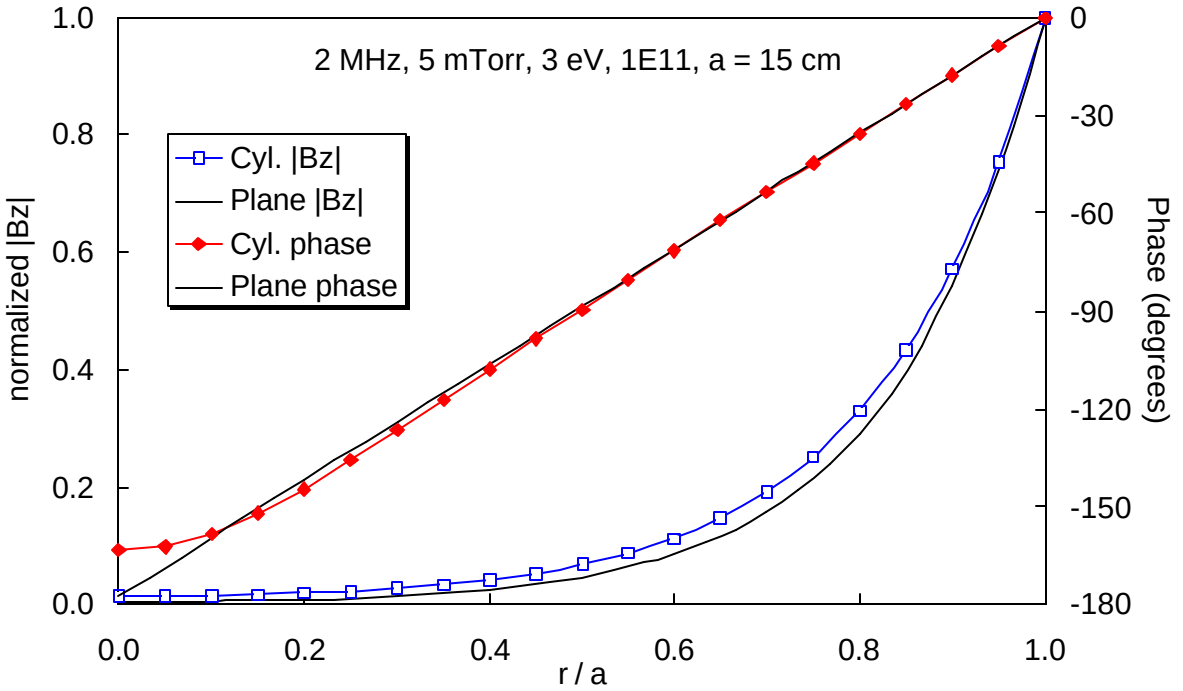

Fig. 9. Effect of cylindrical geometry on field profiles.

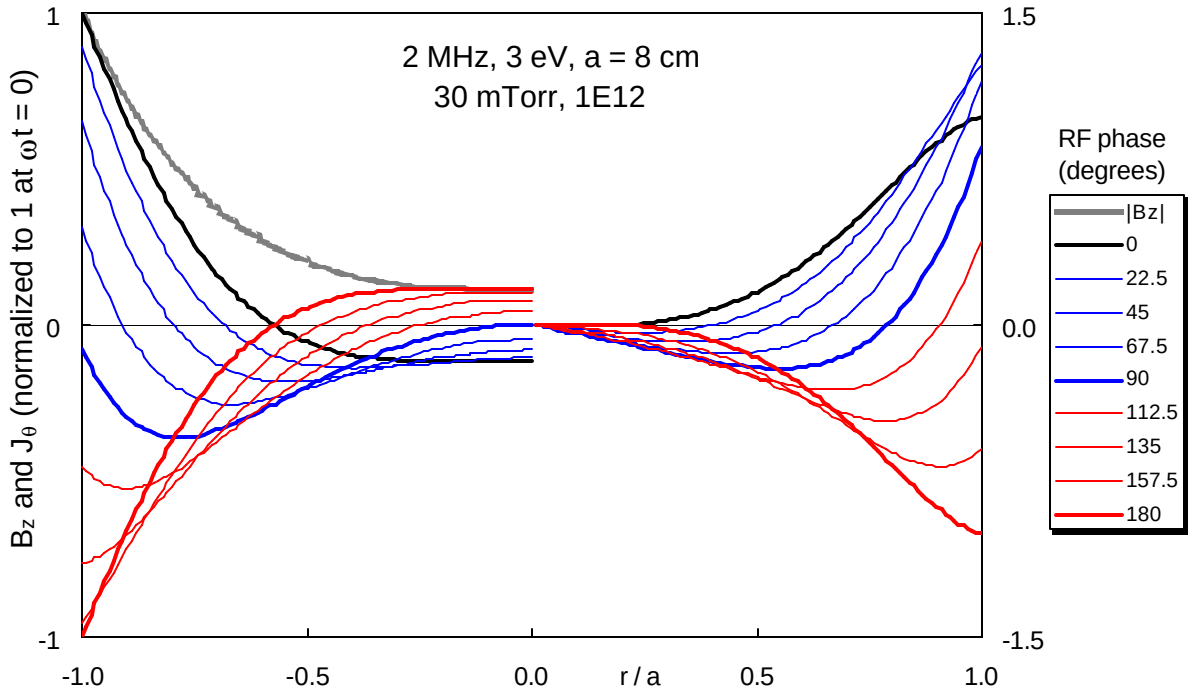

Fig. 10. Instantaneous radial profiles of B_z (left) and J_θ (right) in a case with large ν / ω and d_s / a. The curves are flipped during the second half-cycle. The shaded line is the envelope of the magnitude of B_z.

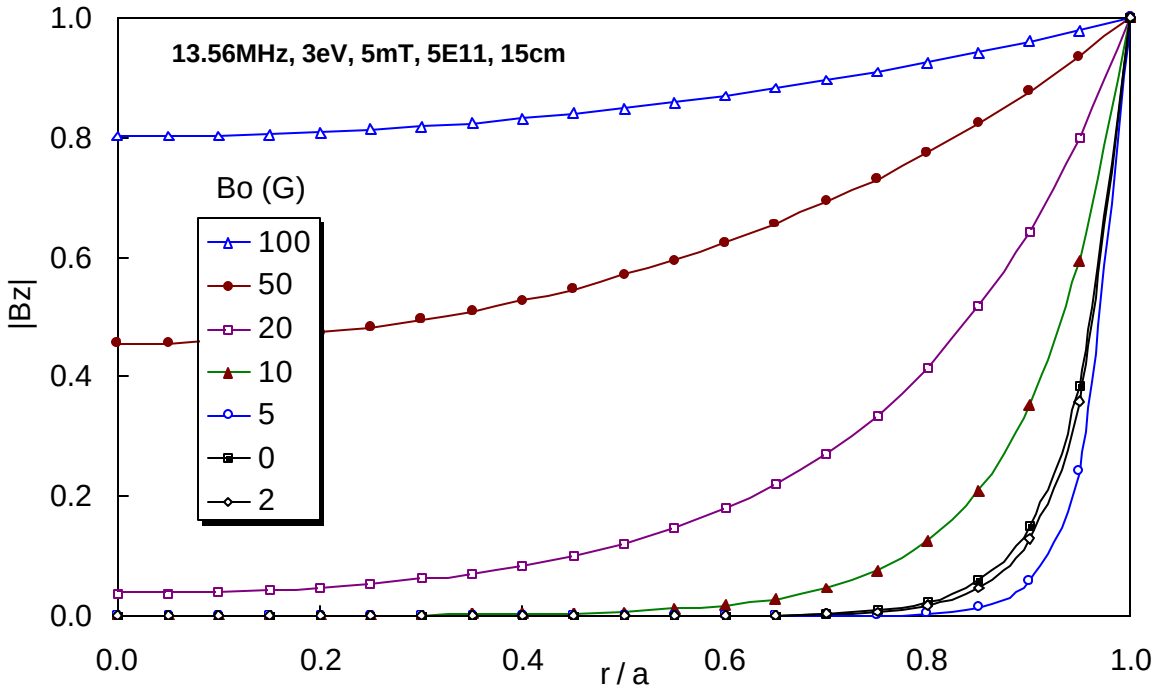

Fig. 11. Effect of an applied DC magnetic field on penetration of a 13.56-MHz RF field into a 15-cm radius cylindrical plasma in the TE approximation. Electron collisions are computed for T_e = 3 eV, $n = 5 \times 10^{11}$ cm^{-3}, and p = 5 mTorr of argon; ion collisions are neglected.

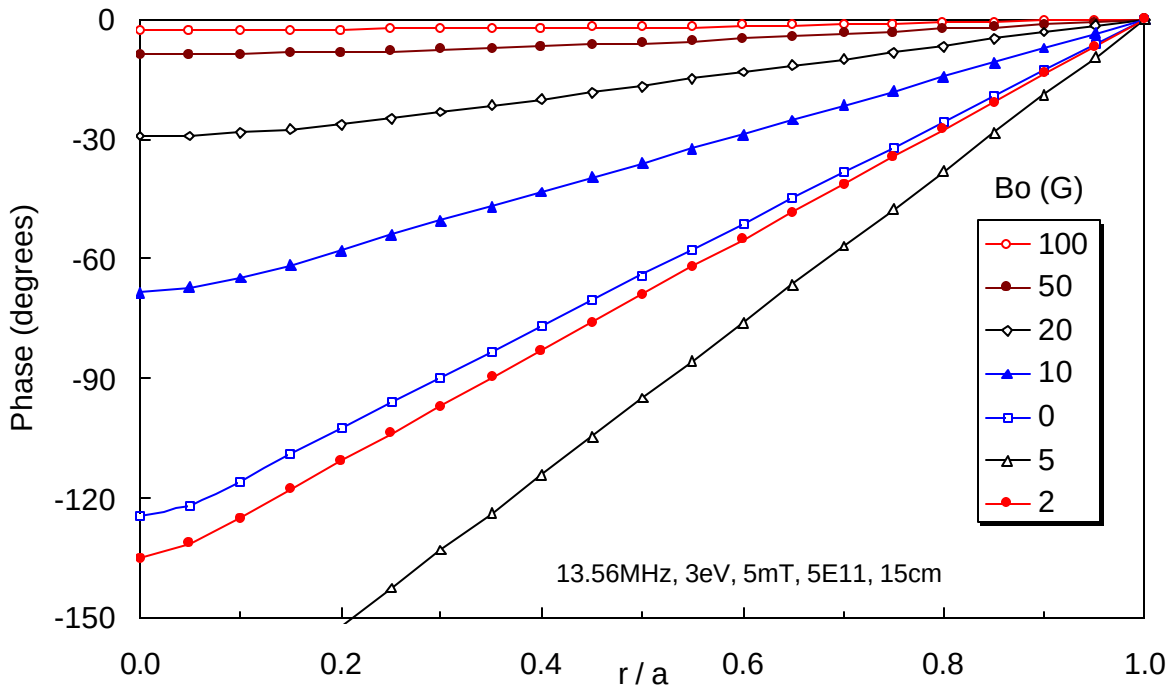

Fig. 12. Relative phase of the RF signal for the case of Fig. 11.

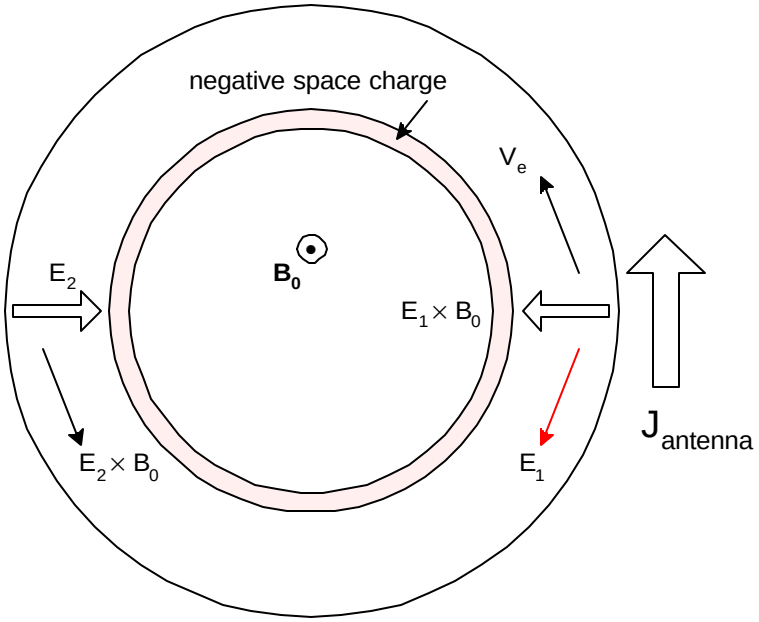

Fig. 13. Physical mechanism of RF penetration across a DC magnetic field.

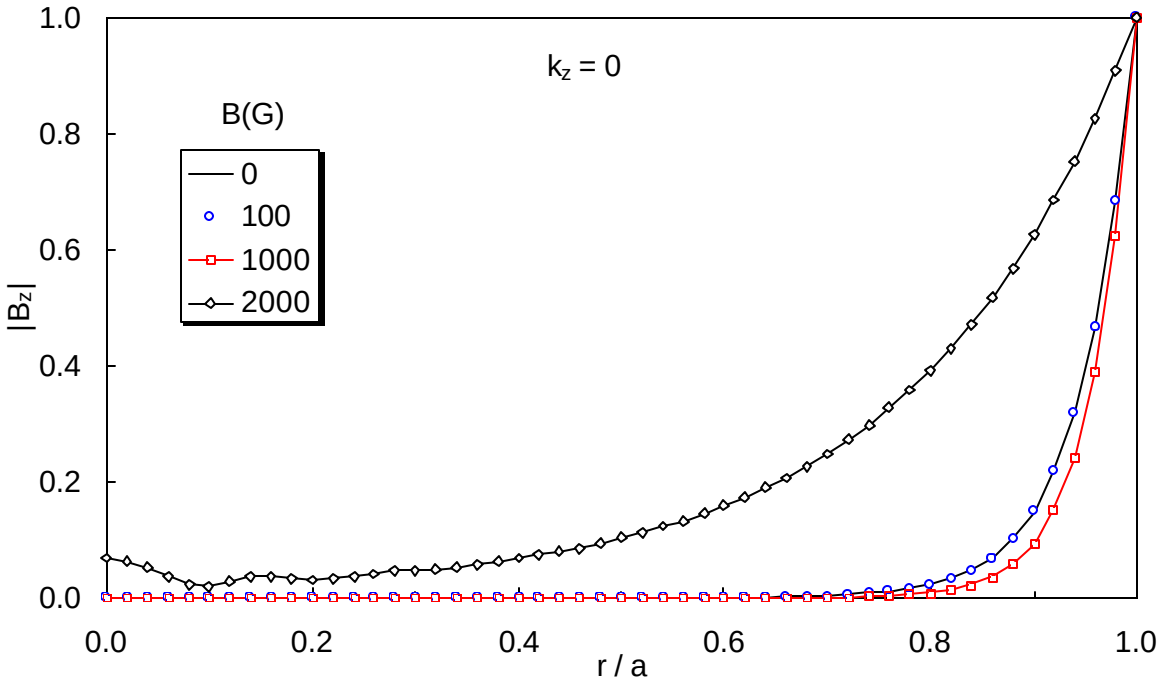

Fig. 14. Computed field magnitude profiles for $k_z = 0$ at various magnetic fields B_0. Conditions are: f = 13.56MHz, T_e = 3eV, p = 5mT, $n = 5 \times 10^{11}$ cm^{-3}, a = 15cm.

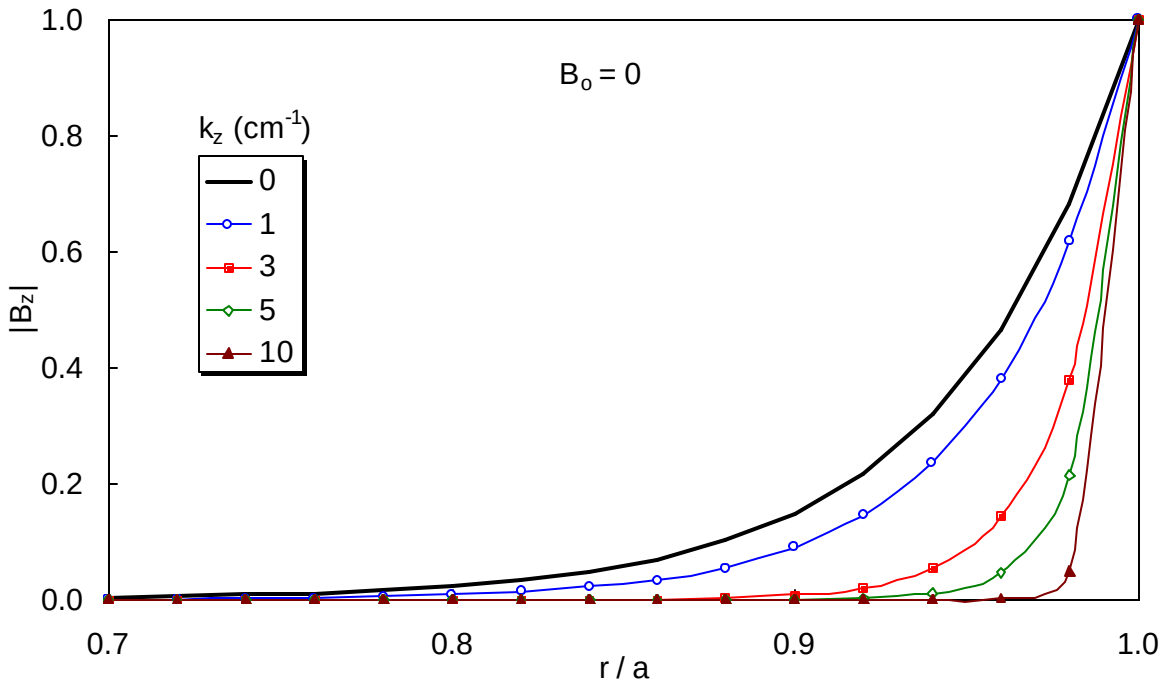

Fig. 15. Computed field magnitude profiles for B_0 = 0 and various values of k_z . Conditions are the same as in Fig. 14.

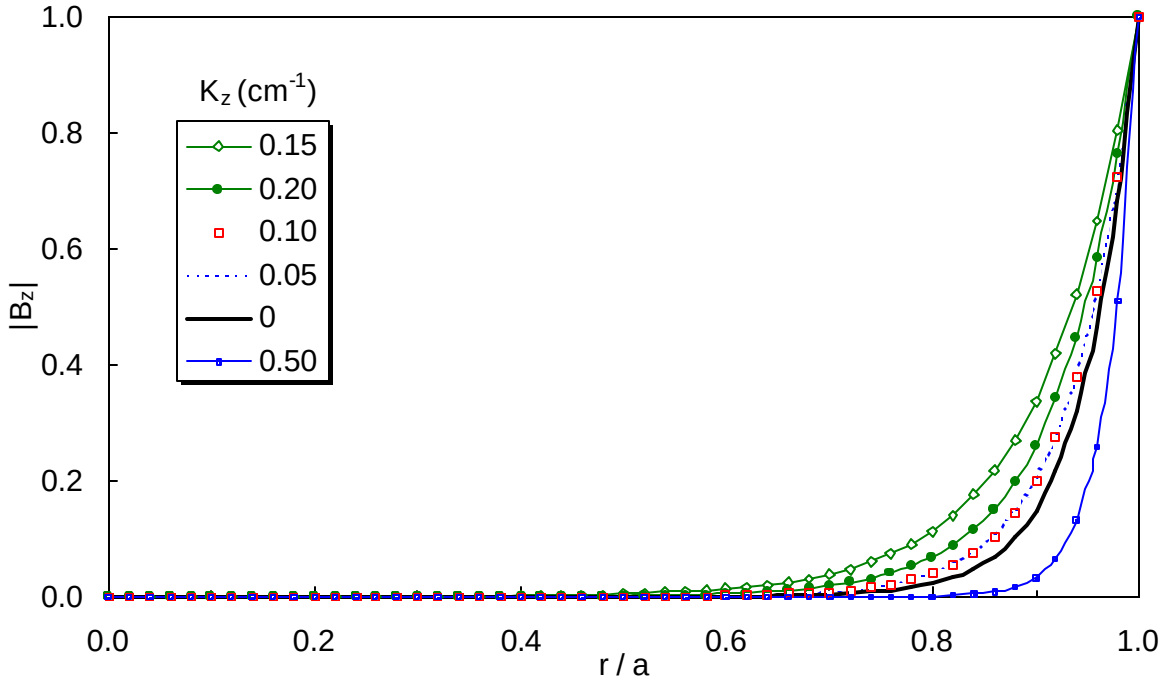

Fig. 16. Computed field magnitude profiles of the TG mode for B_0 = 100 G and various values of k_z . Conditions are the same as in Fig. 14. The variation is not monotonic; the curves appear in the same order as in the legend.

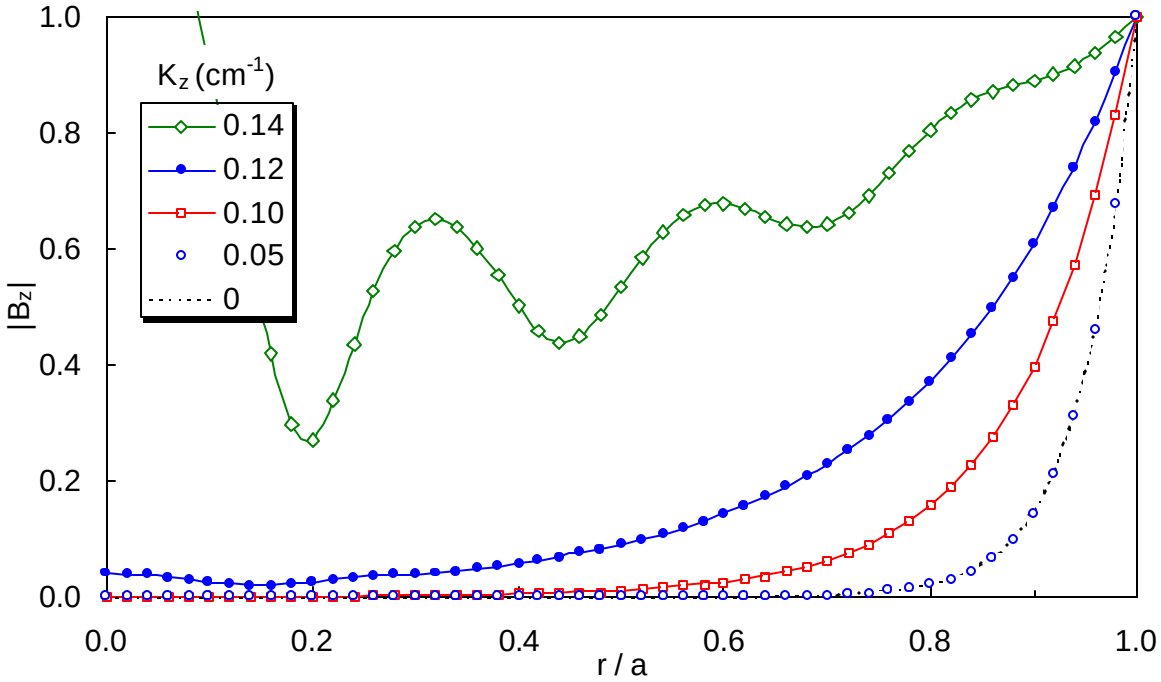

Fig. 17. Computed field magnitude profiles of the helicon mode for B_0 = 100 G and various values of k_z . Conditions are the same as in Fig. 14.

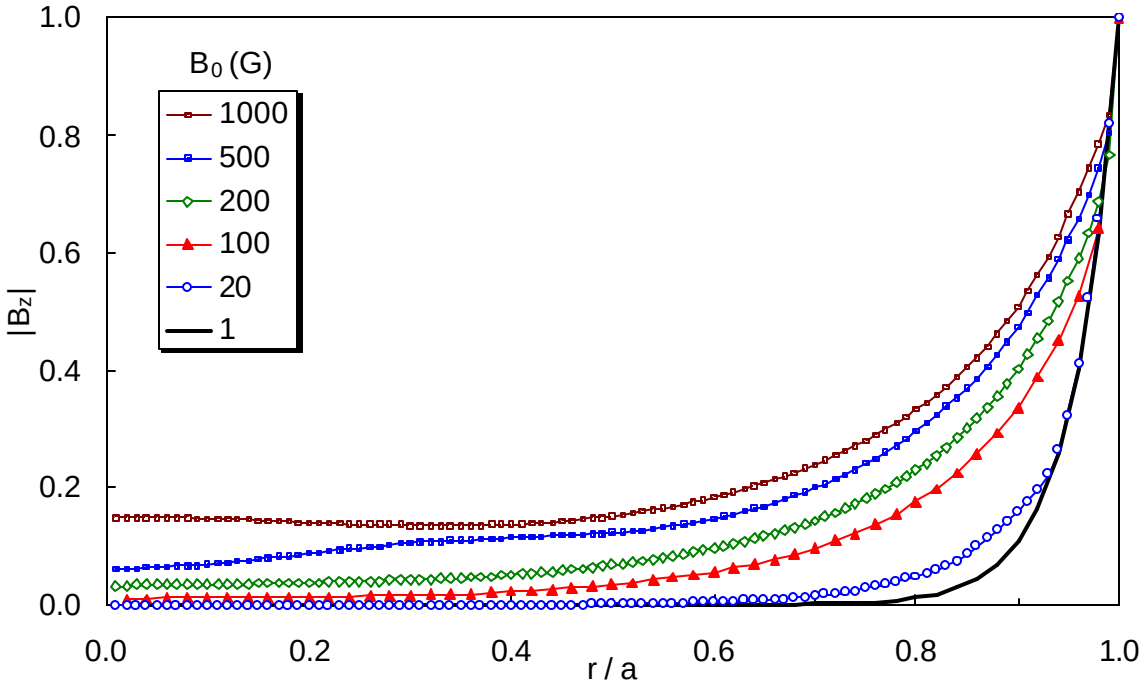

Fig. 18. Exact calculations of field profiles at various magnetic fields using the HELIC code. The antenna is a simple loop, and plasma conditions are the same as in Fig. 14.

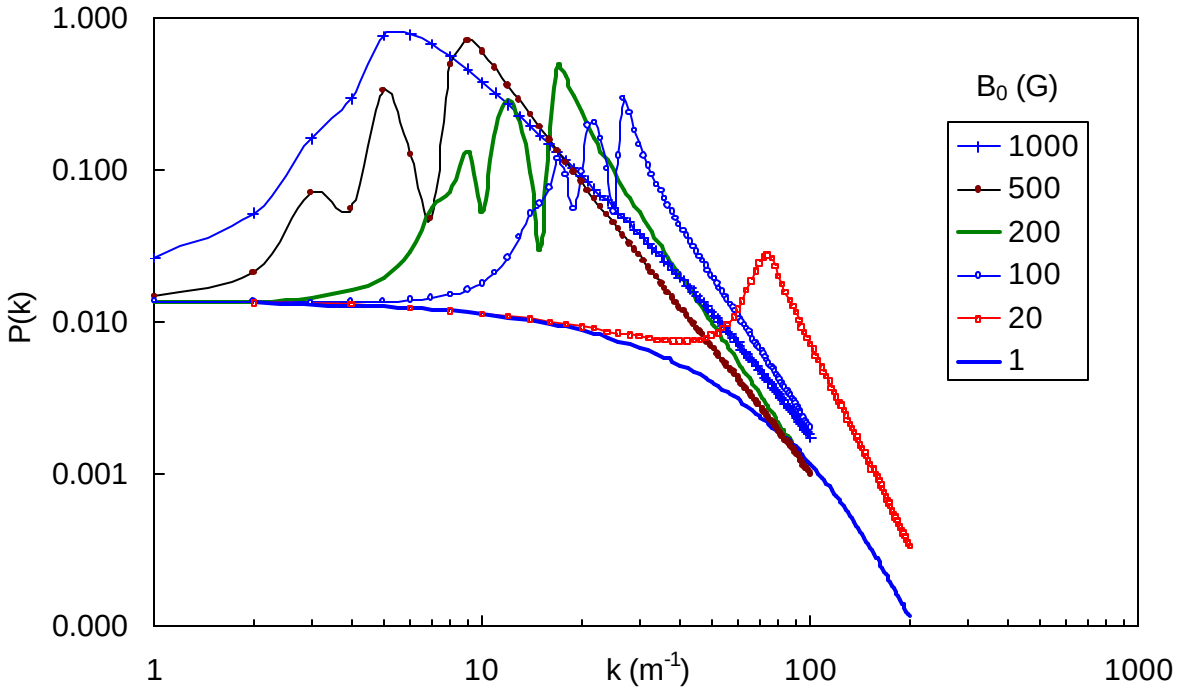

Fig. 19. The spectrum $P(k_z)$ of power deposited per unit k corresponding to the curves on Fig. 17. Logarithmic scales are used because the coupling efficiency is two orders of magnitude lower at low B_0 fields corresponding to ICP operation. The peaks at high fields correspond to eigenmodes of the coupled helicon-TG waves.

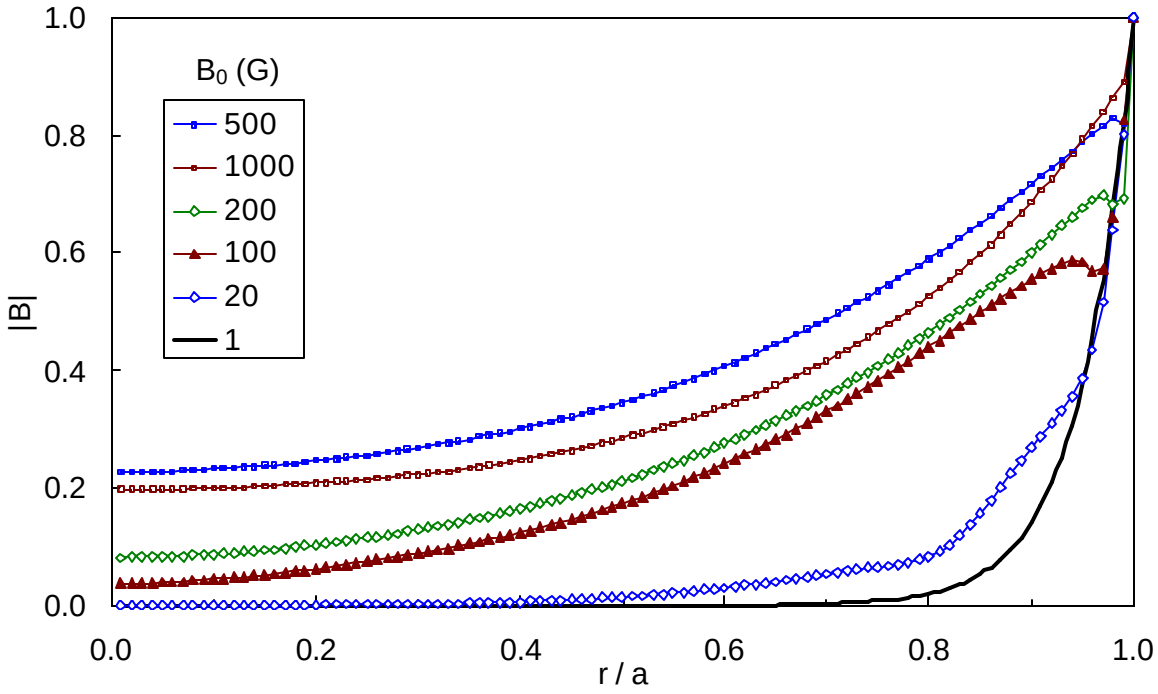

Fig. 20. Same as Fig. 18 except that the antenna is a half-wavelength helix with $m = 1$ symmetry, and the total $|\mathbf{B}|$ is plotted rather than $|B_z|$.

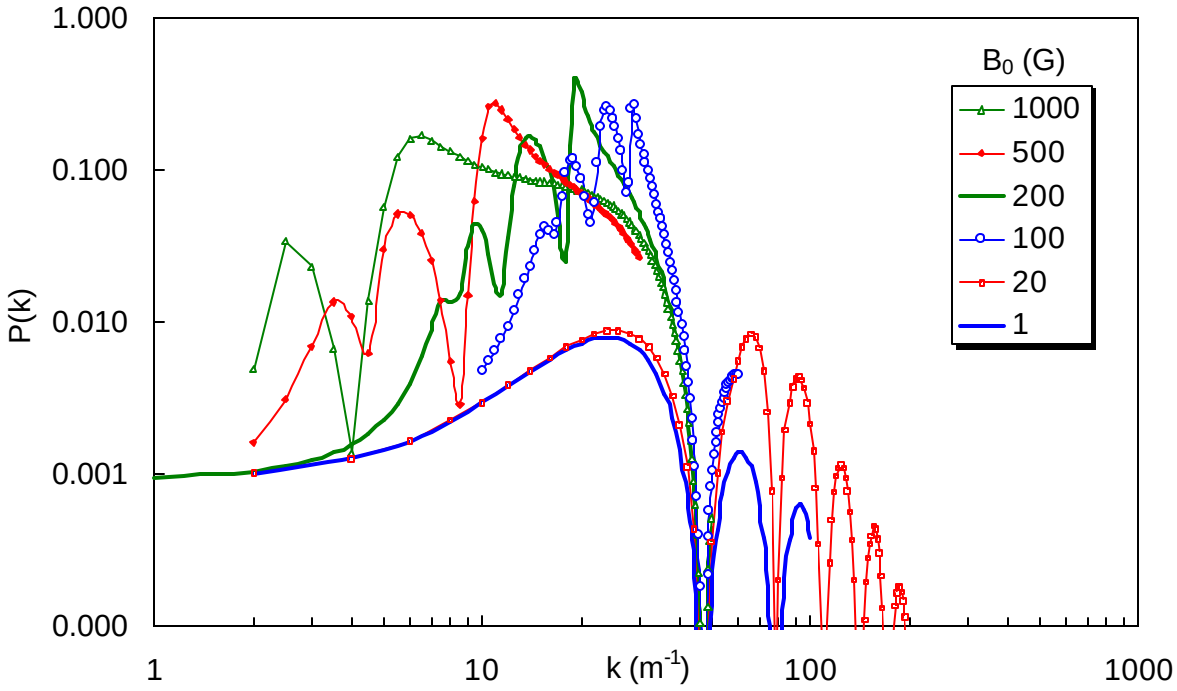

Fig. 21. The spectrum of waves in the plasma producing the field profiles of Fig. 20 at various magnetic fields.